

THE ATACAMA COSMOLOGY TELESCOPE: A MEASUREMENT OF THE $600 < \ell < 8000$ COSMIC MICROWAVE BACKGROUND POWER SPECTRUM AT 148 GHz

J. W. FOWLER¹, V. ACQUAVIVA^{2,3}, P. A. R. ADE⁴, P. AGUIRRE⁵, M. AMIRI⁶, J. W. APPEL¹, L. F. BARRIENTOS⁵, E. S. BATTISTELLI^{7,6}, J. R. BOND⁸, B. BROWN⁹, B. BURGER⁶, J. CHERVENAK¹⁰, S. DAS^{11,1,2}, M. J. DEVLIN¹², S. R. DICKER¹², W. B. DORIESE¹³, J. DUNKLEY^{14,1,2}, R. DÜNNER⁵, T. ESSINGER-HILEMAN¹, R. P. FISHER¹, A. HAJIAN^{2,1}, M. HALPERN⁶, M. HASSELFIELD⁶, C. HERNÁNDEZ-MONTEAGUDO¹⁵, G. C. HILTON¹³, M. HILTON^{16,17}, A. D. HINCKS¹, R. HLOZEK¹⁴, K. M. HUFFENBERGER¹⁸, D. H. HUGHES¹⁹, J. P. HUGHES³, L. INFANTE⁵, K. D. IRWIN¹³, R. JIMENEZ²⁰, J. B. JUIN⁵, M. KAUL¹², J. KLEIN¹², A. KOSOWSKY⁹, J. M. LAU^{21,22,1}, M. LIMON^{23,12,1}, Y.-T. LIN^{24,2,5}, R. H. LUPTON², T. A. MARRIAGE², D. MARSDEN¹², K. MARTOCCI^{25,1}, P. MAUSKOPF⁴, F. MENANTEAU³, K. MOODLEY^{16,17}, H. MOSELEY¹⁰, C. B. NETTERFIELD²⁶, M. D. NIEMACK^{13,1}, M. R. NOLTA⁸, L. A. PAGE¹, L. PARKER¹, B. PARTRIDGE²⁷, H. QUINTANA⁵, B. REID^{20,1}, N. SEHGAL^{21,3}, J. SIEVERS⁸, D. N. SPERGEL², S. T. STAGGS¹, D. S. SWETZ^{12,13}, E. R. SWITZER^{25,1}, R. THORNTON^{12,28}, H. TRAC^{29,2}, C. TUCKER⁴, L. VERDE²⁰, R. WARNE¹⁶, G. WILSON³⁰, E. WOLLACK¹⁰, Y. ZHAO¹

Draft version November 9, 2018

ABSTRACT

We present a measurement of the angular power spectrum of the cosmic microwave background (CMB) radiation observed at 148 GHz. The measurement uses maps with $1.4'$ angular resolution made with data from the Atacama Cosmology Telescope (ACT). The observations cover 228 deg^2 of the southern sky, in a $4^\circ 2'$ -wide strip centered on declination 53° South. The CMB at arcminute angular scales is particularly sensitive to the Silk damping scale, to the Sunyaev-Zel'dovich (SZ) effect from galaxy clusters, and to emission by radio sources and dusty galaxies. After masking the 108 brightest point sources in our maps, we estimate the power spectrum between $600 < \ell < 8000$ using the adaptive multi-taper method to minimize spectral leakage and maximize use of the full data set. Our absolute calibration is based on observations of Uranus. To verify the calibration and test the fidelity of our map at large angular scales, we cross-correlate the ACT map to the WMAP map and recover the WMAP power spectrum from $250 < \ell < 1150$. The power beyond the Silk damping tail of the CMB ($\ell \sim 5000$) is consistent with models of the emission from point sources. We quantify the contribution of SZ clusters to the power spectrum by fitting to a model normalized to $\sigma_8 = 0.8$. We constrain the model's amplitude $A_{\text{SZ}} < 1.63$ (95% CL). If interpreted as a measurement of σ_8 , this implies $\sigma_8^{\text{SZ}} < 0.86$ (95% CL) given our SZ model. A fit of ACT and WMAP five-year data jointly to a 6-parameter Λ CDM model plus point sources and the SZ effect is consistent with these results.

Subject headings: cosmology: cosmic microwave background, cosmology: observations

¹ Joseph Henry Laboratories of Physics, Jadwin Hall, Princeton University, Princeton, NJ, USA 08544

² Department of Astrophysical Sciences, Peyton Hall, Princeton University, Princeton, NJ USA 08544

³ Department of Physics and Astronomy, Rutgers, The State University of New Jersey, Piscataway, NJ USA 08854-8019

⁴ School of Physics and Astronomy, Cardiff University, The Parade, Cardiff, Wales, UK CF24 3AA

⁵ Departamento de Astronomía y Astrofísica, Facultad de Física, Pontificia Universidad Católica, Casilla 306, Santiago 22, Chile

⁶ Department of Physics and Astronomy, University of British Columbia, Vancouver, BC, Canada V6T 1Z4

⁷ Department of Physics, University of Rome “La Sapienza”, Piazzale Aldo Moro 5, I-00185 Rome, Italy

⁸ Canadian Institute for Theoretical Astrophysics, University of Toronto, Toronto, ON, Canada M5S 3H8

⁹ Department of Physics and Astronomy, University of Pittsburgh, Pittsburgh, PA, USA 15260

¹⁰ Code 553/665, NASA/Goddard Space Flight Center, Greenbelt, MD, USA 20771

¹¹ Berkeley Center for Cosmological Physics, LBL and Department of Physics, University of California, Berkeley, CA, USA 94720

¹² Department of Physics and Astronomy, University of Pennsylvania, 209 South 33rd Street, Philadelphia, PA, USA 19104

¹³ NIST Quantum Devices Group, 325 Broadway Mailcode 817.03, Boulder, CO, USA 80305

¹⁴ Department of Astrophysics, Oxford University, Oxford, UK OX1 3RH

¹⁵ Max Planck Institut für Astrophysik, Postfach 1317, D-85741 Garching bei München, Germany

¹⁶ Astrophysics and Cosmology Research Unit, School of Mathematical Sciences, University of KwaZulu-Natal, Durban, 4041, South Africa

¹⁷ Centre for High Performance Computing, CSIR Campus, 15 Lower Hope St., Rosebank, Cape Town, South Africa

¹⁸ Department of Physics, University of Miami, Coral Gables, FL, USA 33124

¹⁹ Instituto Nacional de Astrofísica, Óptica y Electrónica (INAOE), Tonantzintla, Puebla, Mexico

²⁰ ICREA & Institut de Ciències del Cosmos (ICC), University of Barcelona, Barcelona 08028, Spain

²¹ Kavli Institute for Particle Astrophysics and Cosmology, Stanford University, Stanford, CA, USA 94305-4085

²² Department of Physics, Stanford University, Stanford, CA, USA 94305-4085

²³ Columbia Astrophysics Laboratory, 550 W. 120th St. Mail Code 5247, New York, NY USA 10027

²⁴ Institute for the Physics and Mathematics of the Universe, The University of Tokyo, Kashiwa, Chiba 277-8568, Japan

²⁵ Kavli Institute for Cosmological Physics, 5620 South Ellis Ave., Chicago, IL, USA 60637

²⁶ Department of Physics, University of Toronto, 60 St. George Street, Toronto, ON, Canada M5S 1A7

²⁷ Department of Physics and Astronomy, Haverford College, Haverford, PA, USA 19041

²⁸ Department of Physics, West Chester University of Pennsylvania, West Chester, PA, USA 19383

²⁹ Harvard-Smithsonian Center for Astrophysics, Harvard University, Cambridge, MA, USA 02138

³⁰ Department of Astronomy, University of Massachusetts, Amherst, MA, USA 01003

1. INTRODUCTION

The cosmic microwave background (CMB) radiation captures a view of the universe at only $\sim 400,000$ years after the Big Bang. The angular power spectrum of temperature anisotropies in the CMB has been crucial in developing the current standard cosmological model, in which the universe today contains some 5% baryonic matter, 23% dark matter and 72% dark energy. We refer to this model throughout as the Λ CDM model. The temperature power spectrum has been measured to good precision for multipole moments $\ell \lesssim 3000$. At angular scales with $\ell \lesssim 2000$, the power spectrum matches the predictions of Λ CDM, and it can be used to constrain multiple parameters of the cosmological model (e.g., Dunkley et al. 2009; Brown et al. 2009; Reichardt et al. 2009b; Sievers et al. 2009). The agreement between the current polarization anisotropy measurements and the predictions of Λ CDM cosmology further supports the model (e.g., Dunkley et al. 2009; Brown et al. 2009; Chiang et al. 2009).

At $\ell \gtrsim 3000$, the signal from the primary CMB anisotropy becomes dominated mainly by two populations. The first consists of point source emission from both radio and dusty infrared-emitting galaxies. The second is the population of massive galaxy clusters that give rise to the Sunyaev-Zel'dovich (SZ) effect (Sunyaev & Zel'dovich 1970), in which CMB photons scatter off the electrons of the hot intra-cluster medium. Removal of the brightest foreground galaxies and SZ clusters can reduce their contributions to the power spectrum, but the net anisotropy power due to unidentified sources still dominates the exponentially falling primary anisotropy spectrum at small scales.

The top panel of Figure 1 shows recent measurements of the anisotropy at $\ell > 2000$. In analyses of 30 GHz data, radio point sources are masked out and a residual component is modeled and subtracted. For 150 GHz analyses, radio sources are masked and the residual radio and dusty galaxy contribution is estimated.

The SZ effect has a unique frequency signature. In CMB temperature units (the units of Figure 1) the amplitude at 150 GHz is roughly half that at 30 GHz. The amount of SZ power is governed by σ_8 , which measures the amplitude of the cosmic matter power spectrum on $8h^{-1}$ Mpc scales; the SZ power scales approximately as $\sigma_8^7(\Omega_b h)^2$ (Seljak et al. 2001; Komatsu & Seljak 2002). At 30 GHz, CBI reports (Sievers et al. 2009) excess emission above the Λ CDM model at $\ell \approx 3000$ after accounting for all known radio sources (Mason et al. 2009). A possible source of the ‘‘CBI excess’’ is the SZ effect. The SZA data (Sharp et al. 2009), also at 30 GHz and also after accounting for point sources, are consistent with the Λ CDM model at $\ell = 4000$. The ACBAR results (Reichardt et al. 2009b) at 150 GHz are consistent with the CBI excess and Λ CDM. Sievers et al. (2009) show that all the above data in the top panel of Figure 1 are consistent, within 95% CL, with Λ CDM plus a SZ contribution of $\sigma_8 = 0.922 \pm 0.047$ (1σ error bars). Recently, the South Pole Telescope (SPT) group reported $\sigma_8 = 0.773 \pm 0.025$ based on the power spectrum at 150 and 220 GHz (Lueker et al. 2009).

In this paper, we present a new measurement of the CMB anisotropy power spectrum in the range $600 < \ell <$

8000 (corresponding to angular scales of approximately $1.4'$ to $18'$). The observations were made at 148 GHz in 2008 with the Atacama Cosmology Telescope. Figure 1 (bottom panel) shows the results, which are discussed in Section 7. We briefly describe the instrument, the observations, the calibration of the data, and the map-making procedure. The dynamic range of the power spectrum is large enough that we employ new techniques in spectral estimation. We confirm that difference maps of the data give power spectra consistent with no signal and that the power spectrum is insensitive to several details of our analysis. We use the shape of the power spectrum to bound the dusty galaxy contribution and the power from SZ clusters.

2. INSTRUMENT AND OBSERVATIONS

The Atacama Cosmology Telescope (ACT) is a 6-meter, off-axis Gregorian telescope optimized for arcminute-scale CMB anisotropy measurements (Fowler et al. 2007; Hincks et al. 2009). It was installed at an elevation of 5190 m on Cerro Toco¹ in the Atacama Desert of northern Chile in March 2007. Observing conditions in the Atacama are excellent owing to the elevation, the arid climate, and the stability of the atmosphere. After all cuts, the median precipitable water vapor (PWV) was 0.49 mm during the observations presented here.

The Millimeter Bolometer Array Camera (MBAC), the current focal-plane instrument for ACT, uses high-purity silicon lenses to reimaged sections of the Gregorian focal plane onto three rectangular arrays of detectors. The arrays each contain 1000 transition edge sensor (TES) bolometers. Their spectral coverage is determined by metal-mesh filters (Ade et al. 2006) having measured band centers of 148 GHz, 218 GHz, and 277 GHz. The bolometers are cooled to 300 mK by a two-stage helium sorption fridge backed by commercial pulse-tube cryocoolers. The telescope performance and control systems (Hincks et al. 2008; Switzer et al. 2008), camera design (Thornton et al. 2008; Swetz et al. 2008), detector properties (Zhao et al. 2008; Niemack et al. 2008), and readout electronics (Battistelli et al. 2008) are described elsewhere.²

2.1. Observations

ACT operated with all three arrays from mid-August to late December, 2008 for the data presented here. The observing time was divided between two regions away from the galactic plane. The deepest observations cover 900 deg² of the southern sky in a strip 8° wide centered on $\delta = -53^\circ$ with RA from 19^h to 24^h and 0^h to 7^h36^m. The analysis presented in this paper uses only data from the central 228 deg² of the southern strip and only observations made with the 148 GHz array. The slightly elliptical beam has full-widths at half-maximum (FWHM) of $1.40'$ by $1.34'$ at this frequency (Hincks et al. 2009).

The observations were made by scanning the sky at a constant elevation of 50°. Each scan is 4°5' wide on the sky (7°0' in azimuth angle). Scans repeat every 10.2 s. Each half-scan consists of 4.2 s of motion at a constant

¹ ACT is at 22.9586° south latitude, 67.7875° west longitude.

² The site <http://www.physics.princeton.edu/act/> archives papers by the ACT collaboration.

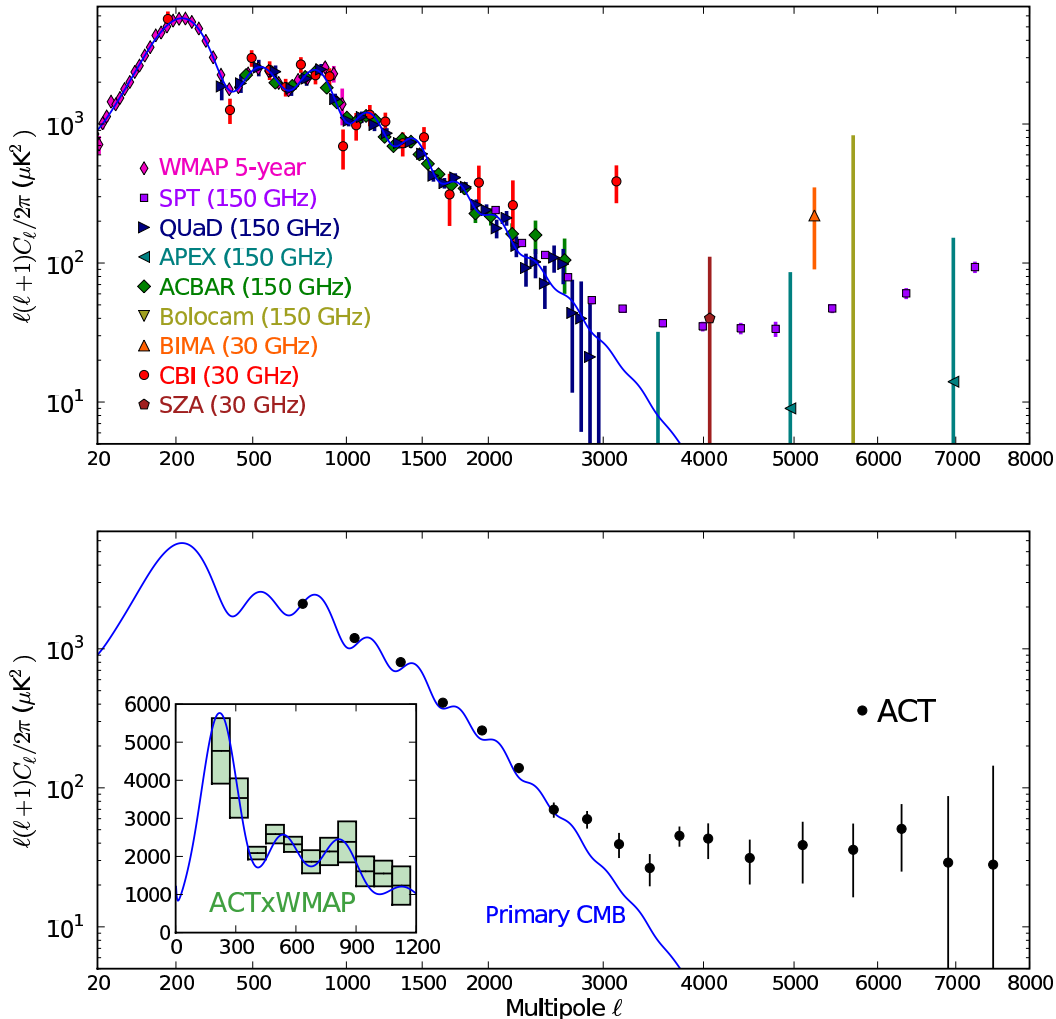


FIG. 1.— Recent measurements of the CMB power spectrum, including this work. *Top*: the measurements of WMAP (Nolta et al. 2009), Bolocam (Sayers et al. 2009), QUaD (Brown et al. 2009; Friedman et al. 2009), APEX-SZ (Reichardt et al. 2009a), ACBAR (Reichardt et al. 2009b), SZA (Sharp et al. 2009), BIMA (Dawson et al. 2006), CBI (Sievers et al. 2009), and SPT (Lueker et al. 2009). For all the results, a radio point source contribution has been removed either by masking before computing the power spectrum (at 150 GHz), or by masking and modeling the residual (at 30 GHz and for WMAP). APEX-SZ additionally masks clusters and potential IR sources. *Bottom*: The ACT power spectrum from this work. The inset shows the cross-power spectrum between ACT and WMAP maps in the ACT southern field (see Section 3.5), which we use to check both the validity of the maps at larger scales and the absolute calibration. Only the ACT power spectrum is analyzed in this paper. In both panels and the inset, the solid curve (blue) is the Λ CDM model of Dunkley et al. (2009) (including lensing). The SZ effect and foreground sources are expected to contribute additional power, as shown in Figure 4 and Table 1. For display purposes—and only in this figure—we scale our result by 0.96 in temperature relative to the Uranus calibration; this calibration factor best fits our data to the Λ CDM model and differs from the Uranus calibration by 0.7σ . Recent WMAP observations of Uranus suggest the same rescaling factor (see footnote to Section 3.2). ACT bandpowers for $\ell > 4200$ have been combined into bins of $\Delta\ell = 600$ for this figure; they are given in a note to Table 1.

speed of $1.5^\circ/\text{s}$ followed by 0.9 s of acceleration. The first half of each night is spent observing the field rising in the eastern sky, after which ACT turns to the western sky to observe the same field as it sets through the standard elevation of 50° . The scan strategy is designed to minimize changes in the telescope’s orientation with respect to the local environment while ensuring cross-linked observations in celestial coordinates. Sky rotation ensures that all detectors sample all points in the field each night,

apart from small areas at the edges.

As the telescope scans in azimuth at constant elevation, each detector is sampled at 399 Hz. The data sampling, position reading, and all housekeeping data are synchronized by a shared 50 MHz clock; absolute times are referenced to a GPS receiver with 0.25 ms accuracy. The data are stored in continuous fifteen-minute segments called time-ordered data sets (TODs). Each TOD requires 1.6 GB of storage per detector array, or 600 MB

after applying lossless compression.

In addition to the main survey, we perform occasional calibration measurements. Most nights, a few minutes are used to measure a planet when it passes through our standard elevation. Any given target is used only once in every three nights to minimize non-uniformity in the coverage of the CMB regions. The planetary observations allow us to measure the system’s relative and absolute responsivities, pointing, and beam profiles; they also provide a way to check for any time variations in each. A series of tuning and biasing procedures are also followed each night before and after regular CMB observations, to optimize and roughly calibrate the detector response.

3. DATA REDUCTION AND MAP-MAKING

The goal of the data reduction is to estimate the maximum-likelihood map of the sky. We select properly tuned detectors and calibrate their pointing and relative gains. The absolute gains are determined by observations of Uranus. The map-making itself is an iterative and computationally intensive process.

3.1. Data selection

The first step in the data reduction is to select TODs when the receiver is cold enough for stable operation and when the precipitable water vapor (PWV) is less than 3 mm. Of the ≈ 2880 h between Aug 25 and Dec 24, 2008, MBAC was on line for 1352 h, roughly corresponding to the night time hours. After cutting on PWV and instrument performance, 1031 h (35% of calendar time) went into the pipeline. Of those, 850 h were spent observing the southern strip.

In the second step of the data reduction, we check whether each detector’s data exhibit problems that warrant removal from the final analysis (Dünner 2009). In the case of rare and transient effects, data are removed for a single detector up to a few seconds at a time; other problems are diagnosed in 15-minute intervals, and when necessary, each detector’s data may be removed for the entire TOD. We check the detector’s response speed; look for transient effects such as cosmic ray hits; and ensure that the feedback loop remained locked, keeping the SQUID amplifiers in the linear regime (Battistelli et al. 2008). Finally, we compare the detector’s response to atmospheric emission with that of the array-wide average, in each case filtering out data at frequencies above 50 mHz. Detectors are cut if their data do not have at least a 0.98 correlation with the average or if the amplitude of the atmospheric signal is not within 15% of the median amplitude found among good detectors. This last cut is the largest and typically removes 100 detectors. Additionally, we bin the data by scan and compute the rms, skewness, and kurtosis in each bin. A cut on rms removes an additional 30 detectors on average, while the combined cut on skewness and kurtosis removes only one additional detector. When the instrument is well-tuned, ACT typically has 680 science-grade detectors at 150 GHz. The remainder are discarded from the analysis or used to monitor instrumental effects. The effective sensitivity of the array, including all instrumental and atmospheric effects, is $\sim 30 \mu\text{K s}^{1/2}$ in CMB temperature units.

3.2. Calibration to planets

After we have a reliable set of detectors to use, the next step is gain calibration. In practice, the cuts are computed twice, so that the final set of cuts is based on calibrated data. We use Uranus as our absolute reference standard.

The atmosphere is an excellent continuous flat-fielding calibrator. We find that the time variation in detector relative responsivities is not significant. Therefore, the detectors’ relative responses to the atmosphere (averaged over the entire season) are used to convert each output to a common scale. Observations of Saturn confirm these relative calibrations; it is the only source observed in 2008 bright enough to use for this confirmation.

We take the brightness temperature of Uranus at 148 GHz to be $T_U = 112 \pm 6$ K (Griffin & Orton 1993; Marten et al. 2005; Kramer et al. 2008). All results in this work scale in proportion to this temperature. For planet calibrations, we use the beam solid angle $\Omega_A = 218 \pm 4$ nsr (Hincks et al. 2009). The net calibration error of 6% in temperature is the combination of these two uncertainties and is dominated by uncertainty in the brightness of Uranus.

Saturn was used as a rough check on the absolute calibration result. The Saturn observations suggest that the ACT data are 10% brighter than inferred from the Uranus data. We attribute this inconsistency to the difficulty in modeling the brightness of the planet and its rings as they vary over time and across frequencies.

We track the stability of the system over time in a number of ways. The absolute celestial calibration is checked through measurements of a planet on most nights. The conversion between raw data and units of power absorbed on the detectors is calibrated in two ways. The conversion is estimated twice nightly by modulating the TES detector bias voltage with a small additional square-wave and measuring the response. A calibration is also performed at the beginning of each night by sweeping all detectors through the full range of bias voltages. Both methods are described further in Niemack (2008) and Fisher (2009). Based on several tests (Switzer 2008), we find that the gain of each detector is constant over the season to better than 2%.

As part of the calibration, the detector temporal response is deconvolved from the detector time streams. We model the response with a single time constant. The detectors’ time constants are determined from the planet measurements and bias steps (Hincks 2009). The median time constant is $\tau_{\text{det}} = 1.9$ ms (thus $f_{3\text{dB}} = 84$ Hz), which corresponds at the ACT scan rate to $\ell \approx 31,000$. Slow detectors with $f_{3\text{dB}} \leq 15$ Hz are not used. We also deconvolve the anti-aliasing filter imposed in the data acquisition system (Battistelli et al. 2008). We then further filter and sample the time stream at half the raw rate to speed the map-making step. This last anti-aliasing filter acts only at angular scales smaller than the beam and does not affect the maps.

3.3. Pointing reconstruction

The planet Saturn is bright enough that each bolometer detects it with high signal-to-noise in a single scan. We fit in the time domain to find the best two-dimensional location for each detector relative to the notional array center. The fit produces altitude and azimuth offsets for each, along with information about

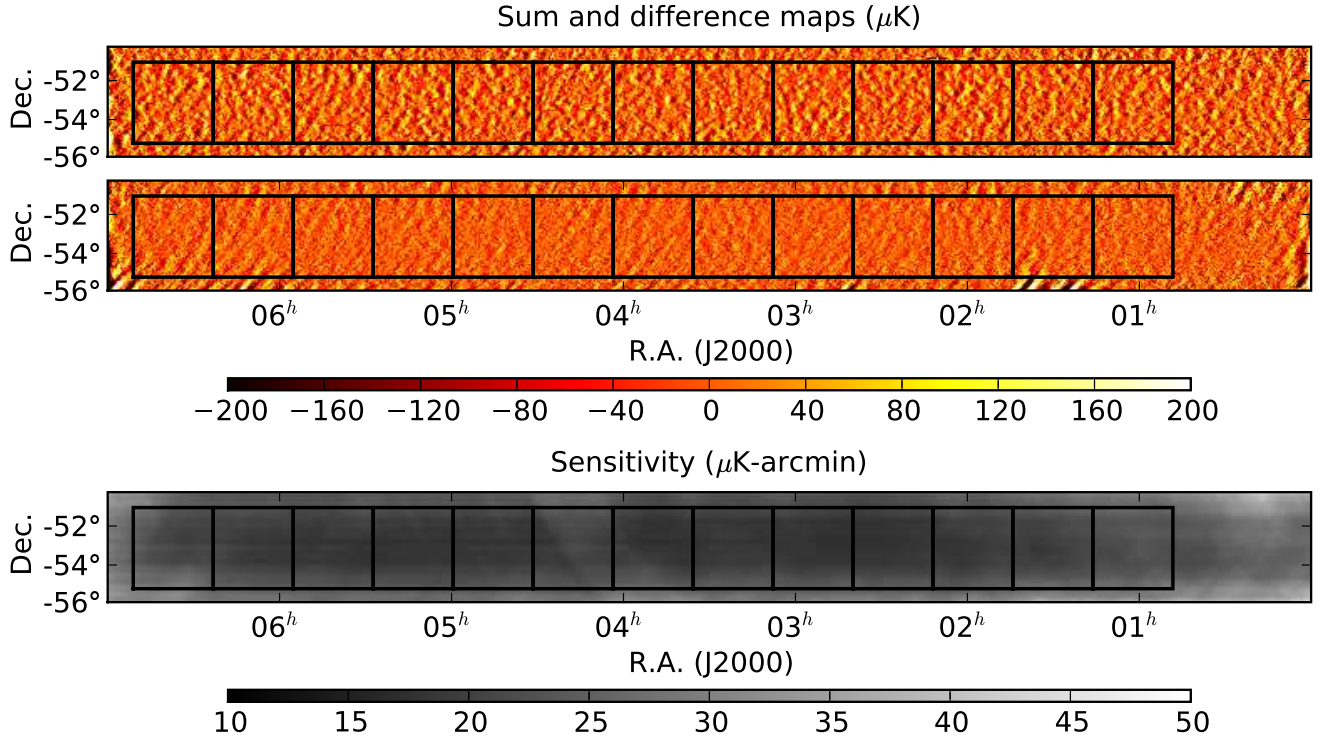


FIG. 2.— The map and a difference map of the ACT southern field at 150 GHz. The same filters used in the power spectrum analysis are applied to both maps: an isotropic high-pass filter suppresses power for $\ell \lesssim 300$ (Equation 2), and all modes with $|\ell_x| < 270$ are set to zero, as described in Section 5.2. *Top*: The ACT southern field. The intensity scale is μK (CMB units). The 360 deg^2 with lowest noise are shown. The squares 4×2 on a side indicate the 13 patches used for the CMB power spectrum analysis (228 deg^2 total). *Middle*: A difference map made from two halves of the same data set. Most of the remaining structure visible at large scales is well below the range of ℓ that we consider in the power spectrum analysis. *Bottom*: The rms temperature uncertainty for one square arcminute pixels.

the relative gains, the beam sizes, and the detector time constants. The detector pointings are consistent with optical models of the telescope and reimaging optics (Fowler et al. 2007). The relative pointing used in this work is an average over 22 observations of Saturn. The rms uncertainty is $1.2''$ for the detector relative pointings, which contributes negligibly to any pointing error in the sky maps.

The location of the array center can also be found from each observation of Saturn. It has a scatter of $4.3''$ rms over the 22 observations, which we attribute to slight thermal deformations in the telescope mirrors and their support structures.

The Saturn data give the absolute location of the array center only for other observations taken at the same horizon coordinates. To determine the absolute location of the array center during science observations, we used approximately 20 known radio sources found in preliminary maps. We find this approach both simpler and better constrained than making a complete pointing model of the telescope. The ACT southern field was observed both rising and setting, at azimuths centered at 30° on either side of south. These preliminary maps were made separately for rising and setting data and were used to determine separate pointing corrections for the two cases. After correction, we estimate the maps to have $5''$ pointing uncertainty.

3.4. Map-making

The goal of the map-making step is to take the 3200 GB of cut, calibrated, and deconvolved raw data from both the rising and setting scans and produce from it a maximum likelihood estimate of the sky. This work produces a 200 MB map, 16,000 times smaller than the raw data set. We first multiply the data for each detector in each TOD by a window function, reducing the weight in the first and last 10 seconds of each file, then remove a single offset and slope for the entire 15-minute period. There is no additional filtering in the time domain, though the lowest frequencies are given no weight in the process of maximizing the likelihood of the final map. The detector data are combined into a data vector \mathbf{d} . The mapping is done in a cylindrical equal-area projection with a standard latitude of $\delta = -53.5^\circ$ and pixels of $30'' \times 30''$, roughly one third of the beam FWHM. The map is represented as a vector \mathbf{m} of length $N_{\text{pix}} \sim 10^7$. We model the data as $\mathbf{d} = \mathbf{P}\mathbf{m} + \mathbf{n}$ where the matrix \mathbf{P} projects the map into the time stream, and \mathbf{n} is the noise, which has covariance matrix \mathbf{N} . The maximum likelihood solution, $\tilde{\mathbf{m}}$, is given by solving the mapping equation (e.g., Tegmark 1997):

$$\mathbf{P}^T \mathbf{N}^{-1} \mathbf{P} \tilde{\mathbf{m}} = \mathbf{P}^T \mathbf{N}^{-1} \mathbf{d}. \quad (1)$$

We solve for $\tilde{\mathbf{m}}$ iteratively using a preconditioned conjugate gradient (PCG) method (Press et al. 2007; Hinshaw et al. 2007). Based on simulations, we find that the solution is an unbiased estimator of the sky for $\ell > 600$, the multipoles that we analyze in this paper. Additionally, the clear cross-correlation with WMAP

(Section 3.5) indicates that the maps are likely unbiased as low as $\ell \approx 200$. This approach is different from that taken by other recent measurements of the fine angular scale anisotropy in which the time stream data are filtered and binned (e.g., Friedman et al. 2009; Reichardt et al. 2009a; Lueker et al. 2009).

Solving Equation 1 requires careful consideration of the noise structure of the ACT data. First, the data are weighted in Fourier space to account for the variation in noise with frequency, particularly to reduce the noise that the atmosphere adds at low frequencies. For frequencies less than 0.25 Hz, we set the statistical weights to zero. Higher frequencies are given successively more weight in inverse proportion to the noise variance in each band. Second, we find that there are several modes, particular combinations of the 1000 detectors, that correspond to signals unrelated to the celestial temperature; for example the common mode, atmospheric gradients, and other detector correlations. We handle them by finding the ten modes with the largest eigenvalues in each TOD and solving for their amplitudes as a function of time along with the map \tilde{m} . The power spectrum (Section 6) is robust to halving or doubling the number of modes.

Maps are made using only fractions of the valid data so that null tests can be performed. The subset maps are also used for finding the CMB power spectrum, as described further in Section 5.2. The final map used for source-finding, however, is a complete run based on all the valid data. Figure 2 shows the map and the region used. The computational task is considerable. One iteration takes 100 seconds on 5000 cores of Canada’s SciNet GPC cluster each running at 2.53 GHz; computations required before the first iteration take an additional time equivalent to approximately twenty iterations. A converged map requires hundreds of iterations and approximately ten CPU years.

3.5. Calibration to WMAP

The absolute calibration described in Section 3.2 is limited by the uncertainty in the 148 GHz brightness of Uranus, the primary calibrator. We complement the planetary calibration by cross-correlating with the W-band (94 GHz) measurements of WMAP (Hinshaw et al. 2009). In the angular scale range of $200 \leq \ell \leq 1200$, both instruments measure the sky with sufficient signal-to-noise to permit the comparison.

The technique requires a single map from WMAP and two maps with independent noise from ACT. We assume that only one relative calibration ratio between ACT and WMAP must be estimated. The WMAP data set consists of the high-resolution³ W-band five-year map. The two independent ACT maps are each made with one half the current data set. We compare the maps only in the 228 deg^2 strip used for the present power spectrum analysis (described in Section 5.1), where the noise is low and uniform.

We compute those cross-spectra in two-dimensional ℓ -space that combine either the full ACT data set with the WMAP map or the two ACT maps with each other. We average over the polar angle in ℓ -space to get a one-dimensional cross-spectrum for each. In the case of the

ACT spectra, the noise is not isotropic, so the spectra are angle-averaged with appropriate weights. We then find the single calibration factor that minimizes χ^2 for a model in which the minimum-variance weighted combination of the ACT-ACT and the ACT-WMAP cross-spectra equals the WMAP all-sky spectrum. The model accounts for the fact that the ACT and WMAP measurements have noise varying as different functions of ℓ .

The result is a calibration factor with $< 6\%$ fractional uncertainty in temperature. The calibration factors derived from WMAP and from Uranus observations are consistent to $\lesssim 6\%$.

4. FOREGROUNDS

Radio and infrared galaxies are the dominant sources of foreground emission in the 150 GHz band at $\ell \geq 1000$. To study the underlying CMB spectrum, the sources must be identified and masked, and residual contamination in the power spectrum must be accounted for. Many approaches to the problem have been described in the CMB literature (e.g., Wright et al. 2009; Reichardt et al. 2009a,b; Sharp et al. 2009; Dawson et al. 2006; Sievers et al. 2009). Our approach is to find the sources in the ACT maps, mask them, and assess the residual contribution with models.

We find the sources using a matched filter with noise weighting derived from the statistical properties of the map (Tegmark & de Oliveira-Costa 1998). We identify as sources all pixels detected at $\geq 5\sigma$ having at least 3 neighboring pixels detected at $\geq 3\sigma$. A 5σ detection corresponds to roughly 20 mJy in the filtered map. The selection criteria are tested on simulated sky maps to determine the sample’s purity and completeness. The sample is approximately 85% complete at 20 mJy and $\sim 100\%$ complete at 50 mJy. For fluxes greater than 20 mJy, the detections have a purity of $\sim 95\%$ (that is, in a hundred detections approximately five are false). Simulations show that at 20 mJy deboosting (Condon 1974) is a $\sim 9\%$ effect, and at 40 mJy a $\lesssim 1\%$ effect.

In the 228 deg^2 area, we detect 108 sources. Of these, 105 can be identified with sources in the PMN (Wright et al. 1994), SUMSS (Mauch et al. 2003), and/or AT20G (Murphy et al. 2009) radio source catalogs. One source, not in these catalogs, is in the 2MASS catalog (and thus has IR emission). Two have no previously measured counterparts. In a $1'$ search radius, 17 sources have both radio and IR identifications. With the exception of the single 2MASS source, all are treated as radio sources.

We fit the flux distribution of the radio sources to three models. The distribution agrees with the Toffolatti et al. (1998) radio model scaled by 0.49 ± 0.12 in source counts, where the uncertainty is statistical only. In the WMAP analysis of sources at 41 GHz, Hinshaw et al. (2007) found a good fit with the same model after scaling the counts by 0.64. Thus it appears that on average the radio population at 150 GHz is composed predominantly of flat-spectrum sources. We prefer to compare the data to models by scaling the model’s flux rather than the counts, as the extrapolation of the radio flux into the 150 GHz range is typically the most uncertain part of any model. For the Toffolatti et al. (1998) model, the required flux scaling is 0.5. The sources are also well fit by the De Zotti et al. (2005) model scaled by 1.2 in flux.

³ The WMAP maps are at HEALPix resolution $N_{\text{side}} = 1024$, with $3.5'$ pixels.

Lastly, we fit the radio sources model in Sehgal et al. (2010) and find that its flux should be scaled by approximately 2.1. All scale factors have a statistical uncertainty of about 25%. Each of these models can be used to estimate the residual rms flux below the 20 mJy cut, as discussed in Section 7.1. We plan a more thorough exploration of the radio sources in an upcoming publication.

Before computing the power spectrum, we mask a $10'$ diameter region around each of the 108 sources. We call this Mask-ACT. In total, 2.3 deg^2 are masked, or 1.0% of the map. Doubling the size of the masked holes has a negligible effect on the power spectrum. We also create a cluster mask, Mask-C, by finding all 5σ clusters and check that using this mask combined with Mask-ACT has a negligible effect on the power spectrum. We also generate a mask, Mask-R, based on known radio sources measured in the SUMSS (0.8 GHz), PMN (5 GHz) and ATCA (20 GHz) catalogs. A model that has been fit to multiple data sets (Sehgal et al. 2010) is used to estimate the mean spectral index, and this index is then used to determine the flux cut in the radio catalogs. Since the model is based on ensemble properties of radio sources it may miss lower-flux low frequency sources having shallow indices. The resulting power spectrum is independent of which radio source mask we use, or if we use the union of the two, and does not depend on whether we include the cluster mask.

Diffuse dust emission becomes dominant near the galactic plane. We check for evidence of dust in the region of our map nearest to the plane, from right ascension 6^{h} to 7^{h} . Through a cross-correlation with the estimated dust map of Finkbeiner et al. (1999) (the FDS map), we can limit the dust contribution here to $\ell(\ell+1)C_\ell/(2\pi) \lesssim 5 \mu\text{K}^2$ at $\ell = 1000$, while a direct power spectrum of the FDS map in the same region gives $\sim 1 \mu\text{K}^2$. As the diffuse dust component decreases with increasing ℓ , it is not significant in our analysis.

5. POWER SPECTRUM METHOD

We estimate the CMB power spectrum using the adaptive multi-taper method (AMTM) with prewhitening, described in Das et al. (2009). We make independent maps from subsets of the data and use only cross-spectra between maps to estimate the final power spectrum. All operations are performed using the flat-sky approximation. We summarize the method in this section.

5.1. Fields used for power spectrum analysis

We find the power spectrum of our map by separate analysis of each of the 13 patches shown in Figure 2. Each patch is 4.2×4.2 in size, and together they cover a rectangular area of the map from $\alpha = 0^{\text{h}}48^{\text{m}}$ to $6^{\text{h}}52^{\text{m}}$ (12° to 103°) in right ascension and from $\delta = -55^\circ16'$ to $-51^\circ05'$ in declination. This area is the region of a larger survey having the lowest noise. We also split the raw data into four subsets of roughly equal size, with the data distributed so that any four successive nights go into different subsets. The four independent maps generated from these subsets cover the same area and have approximately the same depth. All maps are fully cross-linked. That is, they all contain data taken with the sky both rising and setting.

5.2. Spectrum of a single patch

We estimate the spectra of the 13 patches independently, before taking a weighted average to find the final spectrum. There are four independent sky maps, from which six cross-spectra and four auto-spectra are evaluated on each patch. We use a weighted mean of only the cross-spectra for the final spectral estimate. The weights depend on both the cross- and auto-spectra, as discussed below.

Before separating the four maps into 13 patches, each beam-convolved map, $T_b(\boldsymbol{\theta})$, is initially filtered in Fourier space with a high-pass function $F_c(\ell)$. This filter suppresses modes at large scales that are largely unconstrained. These modes arise from a combination of instrument properties, scan strategy, and atmospheric contamination. We choose a squared sine filter, given in Fourier space by the smooth function

$$F_c(\ell) = \begin{cases} 0 & : \ell < \ell_{\min} \\ \sin^2 x(\ell) & : \ell_{\min} < \ell < \ell_{\max} \\ 1 & : \ell > \ell_{\max} \end{cases} \quad (2)$$

where $x(\ell) \equiv (\pi/2)(\ell - \ell_{\min})/(\ell_{\max} - \ell_{\min})$. We choose $\ell_{\min} = 100$ and $\ell_{\max} = 500$. The 13 patches of the map are treated separately from this point. The map of each patch is prewhitened using a local, real-space operation to reduce the dynamic range of its Fourier components (Das et al. 2009). The prewhitening operation involves adding a fraction (2%) of the map to an approximation of its Laplacian. The Laplacian is computed in real space by taking the difference between the map convolved with disks of radius $1'$ and $3'$. Then the maps are multiplied by the point source mask. The prewhitening step greatly reduces the leakage of power from low to high multipoles caused by the action of the point source mask on the highly colored CMB power spectrum.

For each patch, we compute the six 2D cross-spectra and four 2D auto-spectra. The axes correspond to right ascension and declination. Each spectrum is computed using the adaptively weighted multi-taper method, using $N_{\text{tap}} = 5^2$ tapers having resolution parameter $N_{\text{res}} = 3$ (see Das et al. 2009). Windowing the maps with 25 orthogonal taper functions allows us to extract most of the statistical power available in the maps, at the expense of broadening the resolution in angular frequency by a factor of approximately N_{res} . At this stage, each 2D cross-spectrum, $\tilde{C}_\ell^{i\alpha\beta}$, between submaps α and β on patch i incorporates the effects of the filter, prewhitening, tapering, the point source mask, and the beam; they are analogous to a ‘‘pseudo power spectrum’’ of an apodized map (e.g., Hivon et al. 2002). Each 2D spectrum is then averaged in annuli with a narrow range of $|\ell|$ to give the binned pseudo-spectrum $\tilde{\mathcal{B}}_b$, with

$$\tilde{\mathcal{B}}_b^{i\alpha\beta} = P_{b\ell} \tilde{\mathcal{B}}_\ell^{i\alpha\beta}. \quad (3)$$

Throughout this paper we define $\mathcal{B}_\ell \equiv \ell(\ell+1)C_\ell/2\pi$. The binning function $P_{b\ell}$ is set to one for pixels lying in an annular bin (indexed by b) of width $\Delta\ell = 300$ centered on $|\ell| = \ell_b$, and zero elsewhere. The size of the patches and the resolution of the tapers dictates the width of the bins. For our square patches of side $s = 4.2$, the fundamental frequency resolution in Fourier space is $\delta\ell = 2\pi/s \approx 90$. The application of the tapers with a resolution param-

eter $N_{\text{res}} = 3$ further degrades the resolution to $N_{\text{res}}\delta\ell$, so bins chosen to be smaller than $\Delta\ell \sim 270$ would be unavoidably correlated. The binning function is also set to zero where $|\ell_x| < 270$. This region of Fourier space is particularly sensitive to scan-synchronous effects, either fixed to the ground or in phase with the azimuth scan.

The binned pseudo spectrum $\hat{\mathcal{B}}_b^{i\alpha\beta}$ is then deconvolved with the mode-mode coupling matrix, which takes into account the combined effects of tapering and masking and can be computed exactly. Lastly, we divide by the ℓ -space representations of the prewhitening filter, of the high-pass filter $F_c(\ell_b)$, and of the beam to obtain an unbiased estimate of the true underlying spectrum $\mathcal{B}_b^{i\alpha\beta}$.

This procedure has been tested with simulations. The number and resolution of the tapers are chosen as the optimal balance between maximizing information and minimizing bias caused by leakage of power. The simulations confirm that increasing the number of tapers beyond 5^2 has a negligible effect on the spectrum errors.

5.3. Combining patches

The final power spectrum estimator is given by a weighted mean over $N = 13$ patches,

$$\hat{\mathcal{B}}_b = \frac{\sum_{i=1}^N w_b^i \hat{\mathcal{B}}_b^i}{\sum_{i=1}^N w_b^i}, \quad (4)$$

where⁴ $\hat{\mathcal{B}}_b^i \equiv \sum_{\alpha,\beta;\alpha<\beta} \mathcal{B}_b^{i\alpha\beta} / 6$ is the mean of the six deconvolved cross-power spectra in patch i (assuming equal weights), and α and β index the four independent maps of that patch. The weights are chosen as the inverse of the variance of this estimator in each patch, i.e. $w_b^i = 1/\sigma^2(\hat{\mathcal{B}}_b^i)$, where

$$\sigma^2(\hat{\mathcal{B}}_b^i) \equiv \langle (\hat{\mathcal{B}}_b^i)^2 \rangle - \langle \hat{\mathcal{B}}_b^i \rangle^2 \quad (5)$$

and the average is taken over the several cross-spectra computed for patch i . The first term contains the 4-point function of the temperature field and is approximated as,

$$\begin{aligned} \langle (\hat{\mathcal{B}}_b^i)^2 \rangle &\simeq \frac{2}{M(M-1)} \\ &\times \sum_{\substack{\alpha,\beta,\gamma,\delta \\ \alpha<\beta;\gamma<\delta}} (\mathcal{B}_b^{\alpha\beta} \mathcal{B}_b^{\gamma\delta} + \mathcal{B}_b^{\alpha\delta} \mathcal{B}_b^{\beta\gamma} + \mathcal{B}_b^{\alpha\gamma} \mathcal{B}_b^{\beta\delta}), \end{aligned} \quad (6)$$

where $M = 4$ is the number of submaps per patch. We have neglected any connected (non-Gaussian) part of the 4-point function due to components such as point sources. This is a reasonable approximation when choosing the 13 weights, because the expression (Equation 6) is dominated by the auto-spectrum terms, which in turn are noise-dominated.

5.4. Power spectrum covariance

We estimate the bandpower covariance matrix Σ using the scatter in the power spectrum among the $N = 13$ patches,

$$\Sigma_{bb'} \equiv \langle \Delta \mathcal{B}_b \Delta \mathcal{B}_{b'} \rangle \quad (7)$$

⁴ Here we introduce the notation \hat{X} as an unbiased estimator of the quantity X , in the sense $\langle \hat{X} \rangle = X$.

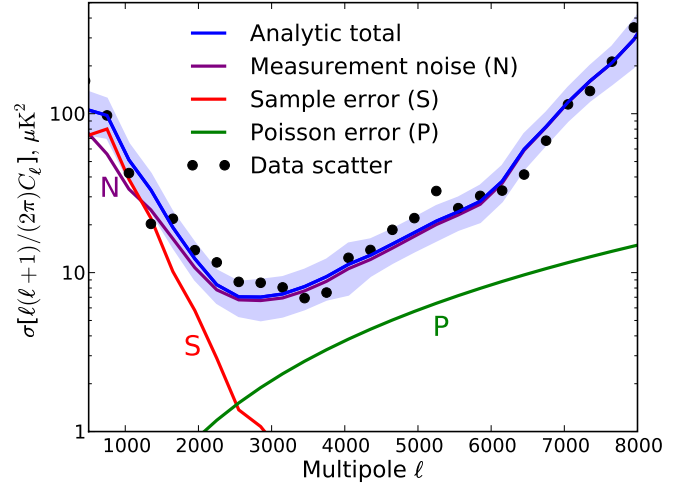


FIG. 3.— The total estimated error σ on the power spectrum (blue) given by the analytic expression (Equations 9 and 10). The uncertainty on σ is found using simulations and is shown by the shaded blue band. The Gaussian sample variance (red line, labeled “S”) dominates for $\ell \lesssim 1200$, and atmospheric plus instrumental noise (purple, “N”) dominates at $\ell > 2000$. The non-Gaussian term due to unmasked point sources and clusters of galaxies contributes about 15% of the variance at $2500 < \ell < 6000$ (green, “P”). The errors estimated using the scatter of the results from the thirteen patches (Equation 8 are shown for comparison (black points); they agree well with the analytic errors.

$$= \frac{\sum_{i=1}^N w_b^i w_{b'}^i \langle (\hat{\mathcal{B}}_b^i - \hat{\mathcal{B}}_b)(\hat{\mathcal{B}}_{b'}^i - \hat{\mathcal{B}}_{b'}) \rangle}{\sum_{i=1}^N w_b^i \sum_{j=1}^N w_{b'}^j}. \quad (8)$$

The square roots of the diagonal elements of the covariance matrix are reported as the errors on our power spectrum estimate.

To test the accuracy of the error estimate, the errors on the power spectrum are also computed analytically. Three terms contribute: sample variance in the CMB multipoles due to limited sky coverage, instrumental and atmospheric noise, and a non-Gaussian term due to unmasked point sources and galaxy clusters. The diagonal component of the variance in one patch can be written as the sum of these terms, in order:

$$\sigma^2(\hat{\mathcal{C}}_b) = \frac{2\hat{\mathcal{C}}_b^2}{n_b} + \frac{4\hat{\mathcal{C}}_b \hat{N}_b / M + \hat{N}_b^2 / n_w}{n_b} + \frac{\sigma_P^2}{f_{\text{sky}}}, \quad (9)$$

where $\hat{N}_b = (\hat{\mathcal{C}}_b^A - \hat{\mathcal{C}}_b)$, the difference between the weighted mean auto- and cross-spectra, estimates the average power spectrum of the noise; $M = 4$ is the number of maps with independent noise properties per patch; $n_w = M(M-1)/2 = 6$ is the number of cross-spectra per patch; n_b counts the number of Fourier modes measured in bin b (that is, the number of pixels falling in the appropriate annulus of Fourier space); f_{sky} is the patch area divided by the full-sky solid angle, 4π steradians; and $\hat{\mathcal{C}}_b$ is the weighted mean cross-spectrum. In the last term, σ_P^2 is given by the non-Gaussian part of the four-point function. Thus

$$\sigma_P^2 = \frac{1}{4\pi} \left[\langle \delta T^4(\hat{n}) \rangle - 3 \langle \delta T^2(\hat{n}) \rangle^2 \right], \quad (10)$$

where T is the temperature map and the average is over

pixels in the map. The term arises from the Poisson-distributed components in the maps, including unresolved point sources and clusters of galaxies. For purposes of the covariance calculation, we assume that such sources are distributed independently of one other. This term is constant as a function of ℓ and is computed from the masked maps with the high-pass filter (Equation 2) applied. The overall variance is given by the weighted mean of the patch variances (Equation 9). The covariance among bins is small in the limit that the four-point term does not dominate, and with bins chosen to be sufficiently large.

Figure 3 shows the three components of the errors. The Gaussian part due to sample variance dominates below $\ell = 2000$; it scales as $C_b/\sqrt{n_b}$. The Poisson term due to the non-Gaussian clusters and unresolved point sources contributes about 15% of the error budget for $2500 \lesssim \ell \lesssim 6000$ but is sub-dominant at all scales. The noise term dominates at $\ell \gtrsim 2000$; atmospheric noise is the main contribution at angular scales of $\ell \lesssim 1000$. As a cross-check of the error estimates, we also plot the errors derived from the scatter of the power spectra from the thirteen patches.

The uncertainty in the analytic errors is shown as the shaded band in Figure 3. It was estimated by Monte Carlo simulations. One thousand patches were simulated with white noise and their power spectra taken by the same methods used on the ACT maps. The results demonstrate that the errors estimated from the scatter among our 13 patches are consistent with the expected uncertainty. The same simulations were used to verify that the covariance between different power spectrum bins (Equation 8) is less than 1%.

6. POWER SPECTRUM RESULTS

The binned estimate of the power spectrum \hat{B}_b is shown in Figures 4 and 1, and bandpowers are given in Table 1. With our method the bandpowers are estimated to have less than 1% correlation with neighboring bins, but the window functions have a small overlap, which we account for in the analysis. At $\ell \lesssim 2500$, the estimated power is consistent with previous observations by ground and balloon-based experiments. The features of the acoustic peaks are not distinguished with the coarse binning, but with the fluctuation band-power measured to 5%, this spectrum offers a powerful probe of cosmological fluctuations at small scales. A clear excess of power is seen at $\ell \gtrsim 2500$ which can be attributed to point sources and, to a lesser extent, to the SZ effect.

The large-scale modes are recovered only after iterating the maps. To test for convergence of noiseless maps, we compute the spectra \hat{C}_b^i of difference maps, between the processed simulation map and input simulated sky, at successive iteration numbers i . To account for differences that are non-uniform between data subsets, we use the auto-spectra. We show that the amplitude of fluctuations in the difference map ($\sqrt{\hat{C}_b^i}$) is small, less than 1% of the amplitude of fluctuations in the input map ($\sqrt{\hat{C}_b}$) at all scales by iteration 500, as shown in Figure 5. To test for convergence in the data, where we do not know the input map, we estimate the maximum change in power between the processed map at iteration i and the final it-

eration, estimated as $2\sqrt{\hat{C}_b^i \hat{C}_b}$ using auto-spectra. Here \hat{C}_b^i is the spectrum of the difference map between iteration i and the final iteration, number 1000. We define the convergence ratio r_c as this change in power given as a fraction of the uncertainty in the power, $\sigma(\hat{C}_b)$, and find it to be sufficiently small (less than 0.5) by iteration 500 at all scales. The cross-correlation with WMAP suggests that the maps are well converged down to $\ell \sim 200$. We do not divide the angular power spectrum by a transfer function at any value of ℓ .

We test the isotropy of the power spectrum by estimating the power as a function of phase $\theta = \tan^{-1}(\ell_y/\ell_x)$. We compute the inverse-noise-weighted two-dimensional pseudo spectrum coadded over map subsets and patches. The mean cross-power pseudo spectrum is shown in Figure 6, indicating the region masked at $|\ell_x| < 270$. The spectrum is symmetric for ℓ to $-\ell$, as it is for any real-valued maps. To quantify any anisotropy, the power averaged over all multipoles in the range $500 < \ell < 8000$ is computed in wedges of $\Delta\theta = 20^\circ$. It is found to be consistent with an isotropic 2D spectrum.

TABLE 1
ANISOTROPY POWER IN BANDS OF WIDTH $\Delta\ell = 300$.
TEMPERATURES ARE IN CMB UNITS.

Central ℓ_b	$\ell(\ell+1)C_b/2\pi$ (μK^2) ^{a,b}	ΛCDM model ^c	SZ model ^d	Source model ^e	Total
750	2317 \pm 98	2106.9	3.6	0.8	2111.2
1050	1313 \pm 42	1204.2	4.6	1.5	1210.3
1350	882 \pm 20	777.3	5.3	2.4	785.0
1650	450 \pm 22	431.9	5.8	3.6	441.3
1950	284 \pm 14	248.3	6.1	5.0	259.5
2250	153 \pm 12	133.8	6.3	6.7	146.8
2550	77 \pm 9	72.3	6.5	8.6	87.4
2850	65 \pm 9	38.0	6.6	10.8	55.3
3150	43 \pm 8	19.8	6.7	13.1	39.6
3450	29 \pm 7	10.3	6.7	15.8	32.7
3750	50 \pm 7	5.3	6.7	18.6	30.6
4050	47 \pm 12	2.9	6.6	21.7	31.2
4350	35 \pm 14	1.6	6.6	25.0	33.2
4650	34 \pm 19	0.9	6.5	28.6	36.0
4950	27 \pm 22	0.6	6.4	32.4	39.4
5250	77 \pm 33	0.4	6.3	36.5	43.1
5550	38 \pm 25	0.3	6.2	40.7	47.3
5850	42 \pm 30	0.2	6.1	45.3	51.6
6150	26 \pm 33	0.2	6.0	50.0	56.2
6450	103 \pm 41	0.1	5.9	55.0	61.1
6750	-30 \pm 68	0.1	5.8	60.3	66.2
7050	209 \pm 115	0.1	5.7	65.7	71.6
7350	60 \pm 139	0.1	5.6	71.4	77.1
7650	-38 \pm 213	0.1	5.5	77.4	83.0
7950	-63 \pm 349	0.1	5.4	83.6	89.1

^aThere is negligible covariance between bins. The maximum-likelihood fit agrees best with ΛCDM if the C_b data given here are multiplied by 0.91.

^bFor comparison with the SPT results of Lueker et al. (2009), we also compute the spectrum with wider bins. For five bins of width $\Delta\ell = 400$ from $3000 < \ell < 5000$, we find 39 ± 6 , 41 ± 7 , 49 ± 10 , 36 ± 12 , and 35 ± 13 . For four bins of width $\Delta\ell = 900$ from $5000 < \ell < 8600$, we find 56 ± 19 , 45 ± 25 , 140 ± 70 , and $80 \pm 250 \mu\text{K}^2$. The ACT data are also shown in Figure 1 with bins of width $\Delta\ell = 600$ starting at $\ell = 4200 - 4800$; the bandpowers are given by 31 ± 11 , 39 ± 18 , 36 ± 19 , 61 ± 26 , 29 ± 58 , and $28 \pm 116 \mu\text{K}^2$.

^cThis and all “model” columns are in the same units as the data: thermodynamic μK^2 .

^dAssumes the best-fit value of $A_{\text{SZ}} = 0.63$.

^eAssumes the best-fit value of $A_p = 11.9$ and uncorrelated Poisson sources.

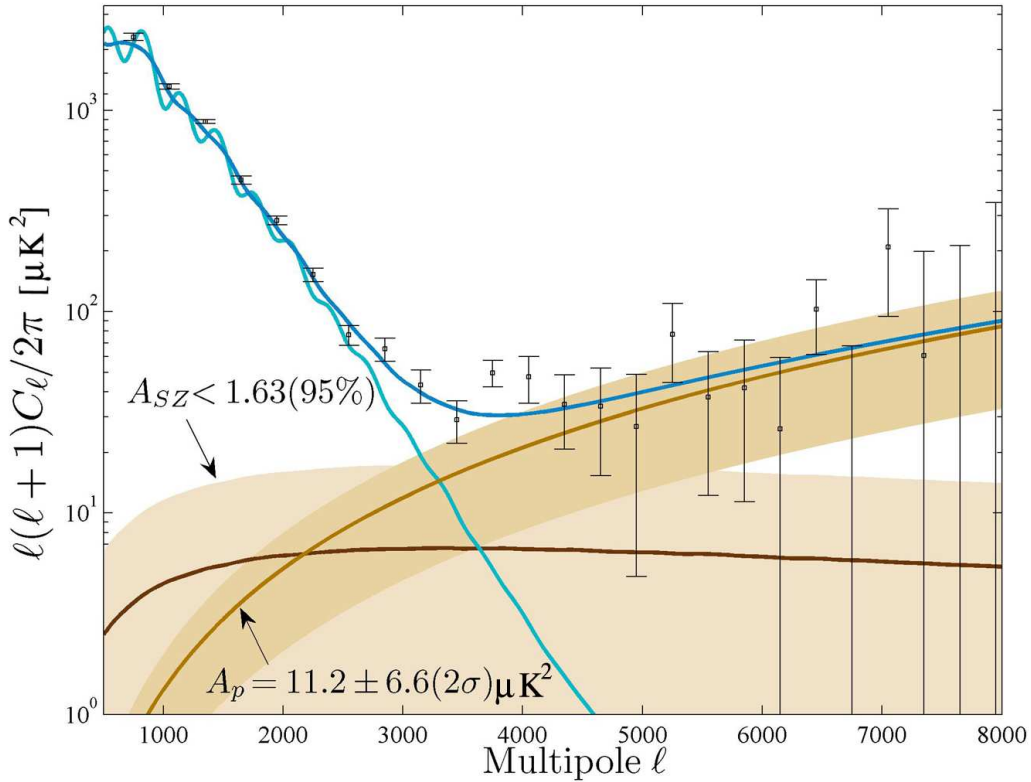


FIG. 4.— The observed power spectrum in bandpowers at 150 GHz from ACT observations (points with error bars). At large angular scales there is good agreement with the lensed Λ CDM model of the primary CMB (light blue curve shown for $\ell < 4700$). The χ^2 of the model is 7.1 for 4 ACT data points in the range $600 < \ell < 1800$. The best-fitting model to the full dataset is shown (dark blue, the highest curve for all $\ell > 2500$). The complete model includes the primary CMB model plus both a Poisson power from point sources and SZ power from clusters; both additional components have been allowed to vary. The complete model has been smoothed by convolution with a boxcar window function of width $\Delta\ell = 300$; the primary CMB model has not been smoothed. The narrower, gold band shows the marginalized 95% CL limits on the Poisson amplitude, while the curve indicates the best-fit amplitude $A_p = 11.9 \mu\text{K}^2$. The wider pink band shows the 95% CL upper bound on the SZ amplitude, $A_{SZ} < 1.63$; the dark curve inside it shows the best-fit value of $A_{SZ} = 0.63$. The Poisson and SZ power are consistent with higher frequency observations and with Λ CDM predictions. The fitting procedure is described in Section 7.

We test that the signals in separate data subsets are consistent by taking the cross-spectrum of two difference maps formed from the temperature maps, T^i , of the four data subsets via:

$$T^{12}(\hat{n}) \equiv [T^1(\hat{n}) - T^2(\hat{n})]/2 \quad (11)$$

$$T^{34}(\hat{n}) \equiv [T^3(\hat{n}) - T^4(\hat{n})]/2. \quad (12)$$

(The data subsets are described in Section 5.1.) The difference maps are expected to contain noise but no residual signal. We estimate the cross-spectrum of the difference maps, $\hat{C}_b = \langle \tilde{T}^{12} \tilde{T}^{34} \rangle$ using the methods described in Section 5 for $M = 2$ data segments. The two other permutations of the data, $\hat{C}_b = \langle \tilde{T}^{13} \tilde{T}^{24} \rangle$, and $\langle \tilde{T}^{14} \tilde{T}^{23} \rangle$ are also tested. The three difference spectra, shown in Figure 7, are consistent with no signal.

7. CONSTRAINTS ON SZ AND IR EMISSION

We perform a simple analysis of the power spectrum to quantify the combined contribution from dusty galaxies and radio sources, and the level of SZ emission. We assume a Λ CDM cosmology with lensing of the CMB and parameters from the five-year WMAP anal-

ysis combined with BAO and supernovae measurements (Komatsu et al. 2009). We defer a full investigation of cosmological parameter constraints until we improve the absolute calibration and better account for astrophysical foregrounds.

Our model for the power at 148 GHz is

$$\mathcal{B}_\ell^{\text{th}} = \mathcal{B}_\ell^{\text{CMB}} + A_{SZ} \mathcal{B}_\ell^{\text{SZ}} + A_p \left(\frac{\ell}{3000} \right)^2 + \mathcal{B}_\ell^{\text{corr}}, \quad (13)$$

where $\mathcal{B}_\ell^{\text{CMB}}$ is the lensed primary CMB power spectrum; $\mathcal{B}_\ell^{\text{SZ}}$ is a template spectrum corresponding to a prediction for the SZ emission in a model with $\sigma_8 = 0.8$ at 148 GHz; A_p quantifies the Poisson point source power, required to be positive; and $\mathcal{B}_\ell^{\text{corr}}$ corresponds to correlated point source power from clustered galaxies. The SZ template we use includes the correlated thermal and kinetic SZ (kSZ) effect derived from numerical simulations and is described in detail in Sehgal et al. (2010). Its amplitude is assumed to scale with σ_8 as the seventh power, such that $A_{SZ} = (\sigma_8^{\text{SZ}}/0.8)^7$ for fixed baryon density. This accounts approximately for the frequency-dependent combination of the thermal SZ component scaling as the 7.5 to 8th power of σ_8 and the sub-dominant kSZ scaling as the fifth power. The expected point source power C_p is

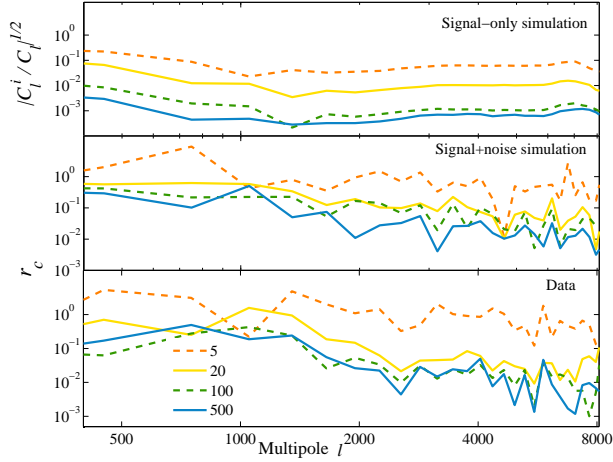


FIG. 5.— Convergence of the maps as a function of iteration. The mapmaking algorithm converges well by iteration 500. For signal-only simulations (*top*), the amplitude of fluctuations in the difference between the processed output map at iteration i and the input map (denoted $(C_b^i)^{1/2}$), is less than 1% of the amplitude of fluctuations in the input map ($\sqrt{C_b}$) at all scales by $i = 500$. Iterations $i = 5, 20, 100$, and 500 are shown. For simulations with noise and for the data (*middle and bottom*, respectively), convergence is tested by estimating the maximum change in power between the processed map at iteration i and iteration 1000, as a fraction of the uncertainty in the power in the final map. For iteration 500 this fraction r_c (described in Section 6) is sufficiently small, less than 0.5 at all scales.

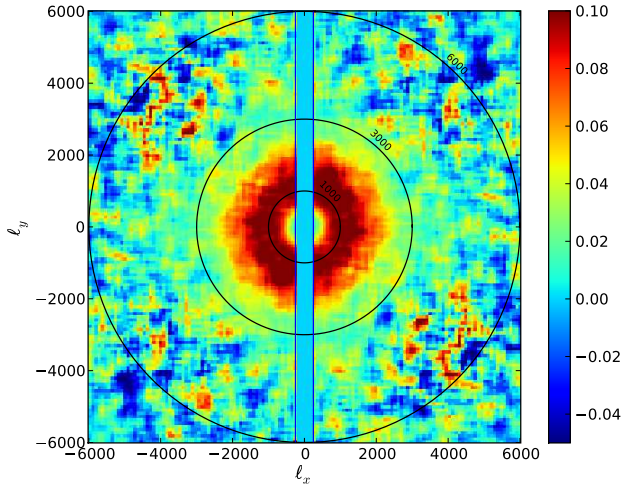


FIG. 6.— The estimated two-dimensional power spectrum C_ℓ , multiplied by a factor of ℓ to emphasize the angular, rather than the radial, variation. The power is consistent with being isotropic, when divided into wedges of $\Delta\theta = 20^\circ$. The vertical lines indicate the narrow region $|\ell_x| < 270$, where excess power from scan-synchronous signals contaminates the power spectrum. This region is not used for the power spectrum analysis. The regions near $(|\ell_x|, |\ell_y|) \approx (4000, 4000)$ are more noisy but not biased. A power spectrum computed without these regions is consistent with the one we present.

given by

$$C_p = g(\nu)^2 \int_0^{S_{\text{cut}}} S^2 \frac{dN}{dS} dS \quad (\mu\text{K}^2 \text{sr}), \quad (14)$$

an integral over all sources with flux S up to some maximum flux S_{cut} , where $g(\nu) \equiv (c^2/2k\nu^2) \times [(e^x - 1)^2/x^2 e^x]$

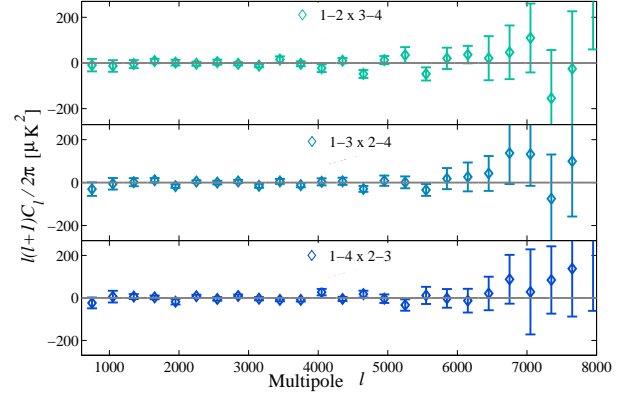


FIG. 7.— Cross-spectra of difference maps formed from four data subsets. In the top panel, two maps $T^{12} \equiv T^1 - T^2$ and $T^{34} \equiv T^3 - T^4$ are formed; both are expected not to contain signal. The cross-spectrum is consistent with no signal. The lower two panels show the same cross-spectra for the other two permutations of the four data subsets and are also consistent with no signal (χ^2 is 25.2, 27.1, and 28.4 in the three panels with 25 degrees of freedom).

converts flux density to thermodynamic temperature, and $x \equiv h\nu/kT_{\text{CMB}}$. Then A_p is the binned $\ell(\ell+1)C_p/2\pi$ Poisson power at pivot $\ell_0 = 3000$. In thermodynamic μK^2 , $C_p = 0.698 \times 10^{-6} A_p$. The conversion to $\text{Jy}^2 \text{sr}^{-1}$ at 148 GHz is $C_p[\text{Jy}^2 \text{sr}^{-1}] = 1.55 C_p[10^{-5} \mu\text{K}^2 \text{sr}]$.

The infrared sources are expected to be clustered. At small angles galaxies cluster with typical correlation function $C(\theta) \propto \theta^{-0.8}$ (e.g., Peebles 1980), which would give $C_\ell \propto \ell^{-1.2}$ on non-linear scales. Motivated by this, we first adopt a simple template for the correlated power,

$$\mathcal{B}_\ell^{\text{corr}} = A_c \left(\frac{\ell}{3000} \right), \quad (15)$$

and fit for the amplitude A_c . Note that on larger scales, $\ell < 300$, $\mathcal{B}_\ell^{\text{corr}}$ is expected to flatten and gradually turn over (e.g., Scott & White 1999), but at these scales at 148 GHz the CMB dominates. Models suggest that the power from source clustering is less than the Poisson component at scales smaller than $\ell = 2000$ (Scott & White 1999; Negrello et al. 2007; Righi et al. 2008). This is consistent with observations at 600 GHz by BLAST (Devlin et al. 2009; Viero et al. 2009). We therefore impose a prior that the correlated power be less than the Poisson power at $\ell = 3000$, i.e., $0 < A_c < A_p$. This model is likely too simplistic, and the correlated power may have an alternative shape (e.g., Sehgal et al. 2010, or the halo model considered in Viero et al. 2009). If the power from dusty galaxies is instead better described by a linear matter power spectrum scaled by a bias factor, $\mathcal{B}_\ell^{\text{corr}}$ becomes almost degenerate with the SZ component $\mathcal{B}_\ell^{\text{SZ}}$ (see, e.g., Hall et al. 2009). Since it is not possible to separate these components with data at a single frequency, our limit on the SZ contribution at 148 GHz should be considered as the upper limit on the sum of the SZ power and a degenerate correlated source power. Multi-frequency data will enable us to investigate the shape and amplitude of the correlated component more fully.

Given this model, the likelihood of the data is given by

$$-2 \ln \mathcal{L} = (\mathcal{B}_b^{\text{th}} - \mathcal{B}_b)^T \Sigma^{-1} (\mathcal{B}_b^{\text{th}} - \mathcal{B}_b) + \ln \det \Sigma, \quad (16)$$

with covariance matrix Σ defined in Equation 8. The

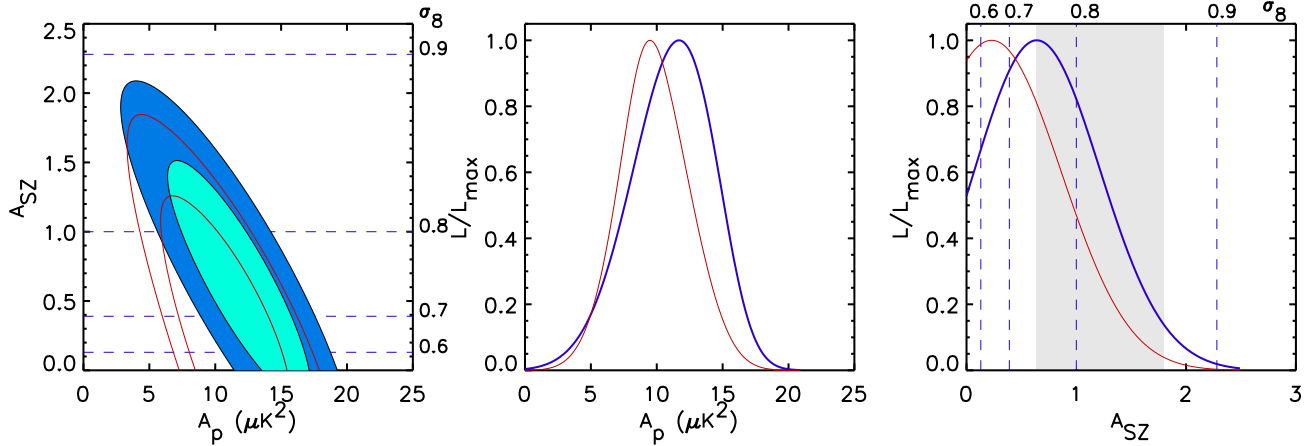


FIG. 8.— Probability distributions for the amplitude A_p of an IR Poisson point source contribution of the form $\mathcal{B}_\ell \equiv \ell(\ell+1)C_\ell/2\pi = A_p(\ell/3000)^2$, and of A_{SZ} , the amplitude of the SZ effect relative to that of a model with $\sigma_8 = 0.80$. Each panel shows two models for the point source power spectrum. In one case, we assume the point sources are uncorrelated Poisson-distributed sources. In the second case, we marginalize over the amplitude of a correlated term scaling as $\mathcal{B}_\ell \propto \ell$. *Left*: The two-dimensional distribution of A_p and A_{SZ} . The filled (blue) regions assume uncorrelated sources; the unfilled (red) regions allow for correlated sources. *Center*: The distribution of A_p marginalized over A_{SZ} . In the center and right panels, the curve peaking at higher amplitude (blue) assumes uncorrelated sources. The point source power is consistent with SCUBA and BLAST data at higher frequencies. *Right*: The distribution of A_{SZ} marginalized over A_p . The shaded region shows the 95% CL limits on σ_8 inferred from WMAP data combined with distance priors.

theoretical spectrum B_b^{th} is computed from the model using $\mathcal{B}_b^{\text{th}} = w_{b\ell}\mathcal{B}_\ell^{\text{th}}$, where $w_{b\ell}$ is an approximate form of the bandpower window function in band b . We marginalize over the calibration uncertainty analytically (Ganga et al. 1996; Bridle et al. 2002).

The uncertainty on the shape of the window function is small, of order 1.5% for the 148 GHz band, compared to 12% overall calibration uncertainty in power. The window uncertainty is therefore neglected throughout this analysis. We verify that this approximation is valid by including the window function uncertainty in the likelihood calculation. The beam Legendre transform is first expanded in orthogonal basis functions, and the uncertainties on the basis function coefficients are used to derive the window function covariance matrix. The covariance is dominated by a small number of modes, so a singular value decomposition is taken. The ten largest modes are included in the likelihood, following the method described in Appendix A of Hinshaw et al. (2007). We find that including the window function uncertainty has only a negligible effect on parameter estimates ($< 0.05\sigma$). The ACT/MBAC beam measurements and the orthogonal function expansion are described in detail in Hincks et al. (2009).

We confirm that the expected values of parameters A_{SZ} , A_p , and A_c are recovered from maps of the ACT simulated sky. We tested simulations with and without noise in the map, and simulations with realistic timestream noise run through the mapper.

In the range $600 < \ell < 1800$, where foreground emission and secondary effects are sub-dominant, the data are consistent with the lensed Λ CDM model alone, with $\chi^2 = 7.1$ for four degrees of freedom (dof). If we rescale the maps to check consistency with the model (multiplying temperatures by 0.96, a 0.7σ change in the calibration), then the χ^2 value becomes 3.0 with 3 dof. We do not rescale the maps in the analysis that follows, though the scale factor is allowed to vary when we marginalized over uncertainties.

Using the full range $600 < \ell < 8100$, we find marginalized constraints on $A_p = 11.2 \pm 3.3 \mu\text{K}^2$ (thus, $C_p = (0.78 \pm 0.23) \times 10^{-5} \mu\text{K}^2$) and $A_{SZ} < 1.63$ (95% CL). The minimum $\chi^2 = 27.0$ for 23 dof. Assuming the scaling of A_{SZ} as $(\sigma_8^{SZ})^7$, this implies an upper limit of $\sigma_8^{SZ} < 0.86$ (95% CL). The one- and two-dimensional distributions are shown in Figure 8, with limits given in Table 2. Marginalizing over the possible SZ power, ACT detects a residual point source component at 3σ ($\delta\chi^2 = 10$). Marginalizing over a correlated term with $A_c < A_p$ gives $A_p = 9.7 \pm 2.8 \mu\text{K}^2$, and $\sigma_8^{SZ} < 0.84$ with $\chi^2 = 26.7$ for 22 dof. Because A_c is forced to be positive, its inclusion has the effect of lowering the limits on A_p and A_{SZ} . Nevertheless, we do not find evidence for a correlated component with current sensitivity levels. The estimated parameters vary by less than 0.6σ when the minimum angular scale is varied in the range $5000 < \ell_{\text{max}} < 8000$, or the SZ template is replaced by the spectrum of Komatsu & Seljak (2002), which is approximately 15% lower than our template in the relevant range of ℓ from 1000–5000. We note that there are multiple models for predicting A_{SZ} (e.g., Bond et al. 2005; Kravtsov et al. 2005) and that the relation between A_{SZ} and σ_8 is an active area of research.

We also combine the ACT spectrum with the WMAP 5-year data (Dunkley et al. 2009) to constrain the six-parameter Λ CDM model (defined by the baryon density, cold dark matter density, cosmological constant, optical depth to reionization, and the amplitude and scale dependence of primordial fluctuations at $k = 0.002 \text{ Mpc}^{-1}$). We model the SZ and point source contribution using Equation 13, neglecting a correlated component. We find similar results for the point source and SZ amplitude in this extended model, with $A_p = 11.5 \pm 3.2$, and $A_{SZ} < 1.66$ (95% CL). The Λ CDM parameters are consistent with WMAP alone, with $100\Omega_b h^2 = 2.27 \pm 0.06$, $\Omega_c h^2 = 0.111 \pm 0.006$, $\Omega_\Lambda = 0.738 \pm 0.030$, $n_s = 0.964 \pm 0.014$, $\tau = 0.086 \pm 0.017$, and $10^9 A_s = 2.4 \pm 0.1$.

TABLE 2
CONSTRAINTS ON SECONDARY ANISOTROPIES AND EXTRA-GALACTIC FOREGROUND EMISSION AT 150 GHz.

	A_{SZ}	σ_8^{SZ}	$A_p(\ell = 3000)$ μK^2	C_p $10^{-5}\mu\text{K}^2$	C_p $\text{Jy}^2\text{sr}^{-1}$	χ^2/dof
Poisson point sources	< 1.63	< 0.86	11.2 ± 3.3	0.78 ± 0.23	1.22 ± 0.36	27.0/23
Poisson + correlated point sources	< 1.36	< 0.84	9.7 ± 2.8	0.68 ± 0.20	1.05 ± 0.30	26.7/22

7.1. Comparison to other point source observations

The residual source level, $C_p = (0.78 \pm 0.23) \times 10^{-5} \mu\text{K}^2$, combines power from radio sources and dusty galaxies that were not removed by the mask. For the three radio source models discussed in Section 4, we expect residual power of $A_p = 6.4 \mu\text{K}^2$ (Toffolatti et al. 1998, after rescaling by 0.4), $A_p = 4.1 \mu\text{K}^2$ (De Zotti et al. 2005), and $A_p = 7 \mu\text{K}^2$ (Sehgal et al. 2010). These models' amplitudes correspond to $C_p^{\text{Radio}} = 0.43, 0.29,$ and $0.49 \times 10^{-5} \mu\text{K}^2$, respectively. The correction for those few sources below 20 mJy that we mask can be neglected; it is smaller than the spread among the models. Given the uncertainties in the models, we subtract the typical model from the total source level and infer that the component from residual IR sources lies in the approximate range $0.2 \lesssim C_p^{\text{IR}} \times 10^5 \lesssim 1 \mu\text{K}^2$.

The ACT result on total point source power is similar to those of APEX at 150 GHz, which finds $C_p = 1.1_{-0.8}^{+0.9} \times 10^{-5} \mu\text{K}^2$ (Reichardt et al. 2009a), of ACBAR ($C_p = 2.7_{-2.6}^{+1.1} \times 10^{-5} \mu\text{K}^2$, Reichardt et al. 2009b), and SPT ($C_p = (0.74 \pm 0.06) \times 10^{-5} \mu\text{K}^2$, Hall et al. 2009). This last measurement employs a lower flux level for removing discrete sources: 6.4 mJy versus our cut at 20 mJy. While this difference means that the C_p presented will contain roughly three times as much power from radio sources as the SPT measurement, we nevertheless find that the total residual power due to point sources is consistent between the two results, given the conservative assumption that at least one-quarter of the point source power observed by ACT is due to dusty galaxies rather than to radio sources.

The IR source models in the literature for 148 GHz make a range of predictions. For example, for sources less than 20 mJy the Lagache et al. (2004) model gives $C_p = 40 \times 10^{-5} \mu\text{K}^2$, the Negrello et al. (2007) model gives $C_p = 1.2 \times 10^{-5} \mu\text{K}^2$, and the Sehgal et al. (2010) model gives $C_p = 17.5 \times 10^{-5} \mu\text{K}^2$. The best agreement comes with the Negrello et al. (2007) model.

The emission from dusty galaxies in the rest frame can be modeled as $S_0(\nu) \propto \nu^\beta B_\nu(T)$, with emissivity index $\beta \sim 1.5$ and Planck function $B_\nu(T)$. The effective index α , where $S(\nu) \propto \nu^\alpha$ ($C_\ell \propto \nu^{2\alpha}$), accounts for the redshift of the sources, the intrinsic temperature variation T , and the index β . SCUBA has observed emission at 850 μm (353 GHz), where we expect a similar population of galaxies to contribute (e.g., Greve et al. 2004, 2008). Using SCUBA galaxy number counts and a model for dN/dS , Scott & White (1999) estimate the Poisson power to be $C_p = 730 \times 10^{-5} \mu\text{K}^2 (190 \text{ Jy}^2\text{sr}^{-1})$ for $S_{\text{cut}} = 50 \text{ mJy}$. Combined with residual IR source

level observed by ACT, this implies an effective spectral index of $\alpha_{150-350}$ between 2.6–3.3. This is consistent with emission from dusty star-burst galaxies at high redshift and in line with predictions by White & Majumdar (2004) and Negrello et al. (2007). It also agrees with the $\alpha = 2.6 \pm 0.6$ index inferred from source fluxes measured with MAMBO (1.2 mm) and SCUBA (850 μm) (Greve et al. 2004), and with $\alpha = 2.3$ measured from AZTEC (1.1 mm) and SCUBA (Chapin et al. 2009). Observations by BLAST at 500 μm (600 GHz) have Poisson power $(2.7 \pm 0.2) \times 10^3 \text{ Jy}^2\text{sr}^{-1}$ (Viero et al. 2009). Combining this with the ACT data leads to an estimate of the effective index $2.7 \lesssim \alpha_{150-600} \lesssim 3.6$, consistent with findings by APEX. The consistency with $\alpha_{150-350}$ suggests that similar populations are being probed at these frequencies, although BLAST is sensitive to a lower redshift range than ACT.

7.2. Comparison to other SZ observations

The ACT constraints on the SZ power indicate an amplitude of fluctuations $\sigma_8^{SZ} < 0.86$ (95% CL). This result is consistent with estimates that combine the primordial CMB anisotropy with distance measures, $\sigma_8 = 0.81 \pm 0.03$ (Komatsu et al. 2009), and improves on SZ-inferred limits at 150 GHz from Bolocam ($\sigma_8^{SZ} < 1.57$) (Sayers et al. 2009), Boomerang ($\sigma_8^{SZ} < 1.14$ at 95% CL) (Veneziani et al. 2009), and APEX ($\sigma_8^{SZ} < 1.18$) (Reichardt et al. 2009a). We do not see evidence for an excess of SZ power, in contrast to lower frequency observations by CBI at 30 GHz which prefer a value 2.5σ higher than the concordance value ($\sigma_8^{SZ} = 0.922 \pm 0.047$, Sievers et al. 2009).

The ACT result is also consistent with the recently reported $\sigma_8^{SZ} = 0.773 \pm 0.025$ ($A_{SZ} = 0.42 \pm 0.21$) from the South Pole Telescope (Lueker et al. 2009). The SPT team prefers a form for the correlated point sources that is covariant with the SZ template in the $\ell = 3000$ range (Hall et al. 2009). If such a form is correct, then the A_{SZ} we report should be interpreted as an upper limit on correlated point sources plus the SZ effect. Analysis of the ACT's 218 and 277 GHz data will shed light on possible forms of the correlated component.

The ACT results on σ_8 are also consistent with several recent studies based on the analysis of ROSAT X-ray flux-selected clusters. We note that these X-ray cluster studies themselves are consistent with measures of σ_8 from richness or weak-lensing selected cluster samples (see references in the three articles cited here). Henry et al. (2009) find $\sigma_8(\Omega_m/0.32)^{0.30} = 0.86 \pm 0.04$ (for $\Omega_m < 0.32$) using cluster gas temperatures measured with the ASCA satellite. Vikhlinin et al. (2009) obtain $\sigma_8(\Omega_m/0.25)^{0.47} = 0.813 \pm 0.013$ (stat) ± 0.024 (sys) using temperatures derived from Chandra observations. Simi-

larly, Mantz et al. (2009) find that in spatially flat models with a constant dark energy equation of state, ROSAT X-ray flux-selected clusters yield $\Omega_m = 0.23 \pm 0.04$, $\sigma_8 = 0.82 \pm 0.05$.

After this article was completed, WMAP 7-year measurements of the brightness of Mars and Uranus were released (Weiland et al. 2010). They suggest that $T_U \approx 107$ K, which is $\sim 4\%$ dimmer than the value used here. If the new Uranus temperature is adopted, then all absolute temperatures and source brightnesses in this work would be reduced by 4%, and all C_ℓ values by 8%.

8. CONCLUSIONS

We have presented the first map and the power spectrum of the CMB sky made using data from the Atacama Cosmology Telescope at 148 GHz. With this map we can compare to WMAP at degree angular scales and measure point sources with a resolution of 0.02 . With an unbiased estimator, we extract the power spectrum, C_ℓ , over a range of power exceeding 10^4 .

We have interpreted the spectrum with a simple model composed of the primary CMB, a possible SZ contribution, and uncorrelated point sources. This analysis provides a new upper bound on the SZ signal from clusters ($\sigma_8^{SZ} < 0.86$ at 95% CL, though this is subject to uncertainty in the SZ models). A coordinated program of X-ray, optical, infrared, and millimeter-wavelength observations of the largest SZ clusters is underway.

These high angular resolution measurements probe the microwave power spectrum out to arcminute scales. Above $\ell \sim 2500$, the spectrum is sensitive to non-linear processes such as the formation of galaxy clusters and dusty galaxies. On the low- ℓ end, the spectrum measures the Silk damping tail of the CMB which can be computed using linear perturbation theory as applied to the primordial plasma. It is clear that to understand the $\ell \gtrsim 1000$ end of the primary CMB, and thus to improve significantly on measurements of the scalar spectral index and its running, source modeling will be required. Future analyses of the ACT data will include the two higher-frequency channels and additional sky coverage. In another approach, one can measure the high- ℓ E-modes, because the polarized CMB to foreground ratio is expected to be higher than that for the temperature. We are pursuing both programs, as a polarization-sensitive camera is currently under development.

The ACT project was proposed in 2000 and funded January 1, 2004. Many have contributed to the project since its inception. We especially wish to thank Asad Aboobaker, Christine Allen, Dominic Benford, Paul Bode, Kristen Burgess, Angelica de Oliveira-Costa, Peter Hargrave, Norm Jarosik, Amber Miller, Carl Reintsema, Felipe Rojas, Uros Seljak, Martin Spergel, Johannes Staguhn, Carl Stahle, Max Tegmark, Masao Uehara,

Katerina Visnjic, and Ed Wishnow. It is a pleasure to acknowledge Bob Margolis, ACT's project manager. Reed Plimpton and David Jacobson worked at the telescope during the 2008 season. ACT is on the Chajnantor Science preserve, which was made possible by the Chilean Comisión Nacional de Investigación Científica y Tecnológica. We are grateful for the assistance we received at various times from the ALMA, APEX, ASTE, CBI/QUIET, and NANTEN2 groups. The ATCA team kindly provided the positions of their 20 GHz sources prior to publication. The PWV data come from the public APEX weather website. Field operations were based at the Don Esteban facility run by Astro-Norte. This research has made use of the NASA/IPAC Extragalactic Database (NED) which is operated by the Jet Propulsion Laboratory, California Institute of Technology, under contract with the National Aeronautics and Space Administration. We thank the members of our external advisory board—Tom Herbig (chair), Charles Alcock, Walter Gear, Cliff Jackson, Amy Newbury, and Paul Steinhardt—who helped guide the project to fruition.

This work was supported by the U.S. National Science Foundation through awards AST-0408698 for the ACT project, and PHY-0355328, AST-0707731 and PIRE-0507768. Funding was also provided by Princeton University and the University of Pennsylvania. The PIRE program made possible exchanges between Chile, South Africa, Spain and the US that enabled this research program. Computations were performed on the GPC supercomputer at the SciNet HPC Consortium. SciNet is funded by: the Canada Foundation for Innovation under the auspices of Compute Canada; the Government of Ontario; Ontario Research Fund – Research Excellence; and the University of Toronto.

VA, SD, AH, and TM were supported through NASA grant NNX08AH30G. ADH received additional support from a Natural Science and Engineering Research Council of Canada (NSERC) PGS-D scholarship. AK and BP were partially supported through NSF AST-0546035 and AST-0606975, respectively, for work on ACT. HQ and LI acknowledge partial support from FONDAP Centro de Astrofísica. RD was supported by CONICYT, MECE-SUP, and Fundación Andes. ES acknowledges support by NSF Physics Frontier Center grant PHY-0114422 to the Kavli Institute of Cosmological Physics. KM, M Hilton, and RW received financial support from the South African National Research Foundation (NRF), the Meraka Institute via funding for the South African Centre for High Performance Computing (CHPC), and the South African Square Kilometer Array (SKA) Project. JD received support from an RCUK Fellowship. RH received funding from the Rhodes Trust. SD acknowledges support from the Berkeley Center for Cosmological Physics. YTL acknowledges support from the World Premier International Research Center Initiative, MEXT, Japan. The data will be made public through LAMBDA (<http://lambda.gsfc.nasa.gov/>) and the ACT website (<http://www.physics.princeton.edu/act/>).

REFERENCES

- Ade, P. A. R., Pisano, G., Tucker, C., & Weaver, S. 2006, in Proc. SPIE, ed. J. Zmuidzinas, W. S. Holland, S. Withington, & W. D. Duncan, Vol. 6275, 62750T
- Battistelli, E. S., et al. 2008, in Proc. SPIE, ed. W. D. Duncan, W. S. Holland, S. Withington, & J. Zmuidzinas, Vol. 7020 (SPIE), 702028
- Bond, J. R., et al. 2005, ApJ, 626, 12

- Bridle, S. L., Crittenden, R., Melchiorri, A., Hobson, M. P., Kneissl, R., & Lasenby, A. N. 2002, *MNRAS*, 335, 1193
- Brown, M. L., et al. 2009, *ApJ*, 705, 978
- Chapin, E. L., et al. 2009, arXiv:0906.4561
- Chiang, H. C., et al. 2009, arXiv:0906.1181
- Condon, J. J. 1974, *ApJ*, 188, 279
- Das, S., Hajian, A., & Spergel, D. N. 2009, *Phys. Rev. D*, 79, 083008
- Dawson, K. S., Holzapfel, W. L., Carlstrom, J. E., Joy, M., & LaRoque, S. J. 2006, *ApJ*, 647, 13
- De Zotti, G., Ricci, R., Mesa, D., Silva, L., Mazzotta, P., Toffolatti, L., & González-Nuevo, J. 2005, *A&A*, 431, 893
- Devlin, M. J., et al. 2009, *Nature*, 458, 737
- Dunkley, J., et al. 2009, *ApJS*, 180, 306
- Dünner, R. 2009, Ph.D. thesis, Pontificia Universidad Católica de Chile
- Finkbeiner, D. P., Davis, M., & Schlegel, D. J. 1999, *ApJ*, 524, 867
- Fisher, R. P. 2009, Ph.D. thesis, Princeton University
- Fowler, J. W., et al. 2007, *Appl. Opt.*, 46, 3444
- Friedman, R. B., et al. 2009, *ApJ*, 700, L187
- Ganga, K., Ratra, B., & Sugiyama, N. 1996, *ApJ*, 461, L61
- Greve, T. R., Ivison, R. J., Bertoldi, F., Stevens, J. A., Dunlop, J. S., Lutz, D., & Carilli, C. L. 2004, *MNRAS*, 354, 779
- Greve, T. R., Pope, A., Scott, D., Ivison, R. J., Borys, C., Conzelmann, C. J., & Bertoldi, F. 2008, *MNRAS*, 389, 1489
- Griffith, M. J. & Orton, G. S. 1993, *Icarus*, 105, 537
- Hall, N. R., et al. 2009, arXiv:0912.4315
- Henry, J. P., Evrard, A. E., Hoekstra, H., Babul, A., & Mahdavi, A. 2009, *ApJ*, 691, 1307
- Hincks, A. D. 2009, Ph.D. thesis, Princeton University
- Hincks, A. D., et al. 2008, in *Proc. SPIE*, ed. W. D. Duncan, W. S. Holland, S. Withington, & J. Zmuidzinas, Vol. 7020 (SPIE), 70201P
- Hincks, A. D., et al. 2009, arXiv:0907.0461
- Hinshaw, G., et al. 2007, *ApJS*, 170, 288
- , 2009, *ApJS*, 180, 225
- Hivon, E., Górski, K. M., Netterfield, C. B., Crill, B. P., Prunet, S., & Hansen, F. 2002, *ApJ*, 567, 2
- Komatsu, E. & Seljak, U. 2002, *MNRAS*, 336, 1256
- Komatsu, E., et al. 2009, *ApJS*, 180, 330
- Kramer, C., Moreno, R., & Greve, A. 2008, *A&A*, 482, 359
- Kravtsov, A. V., Nagai, D., & Vikhlinin, A. A. 2005, *ApJ*, 625, 588
- Lagache, G., et al. 2004, *ApJS*, 154, 112
- Lueker, M., et al. 2009, arXiv:0912.4317
- Mantz, A., Allen, S. W., Rapetti, D., & Ebeling, H. 2009, arXiv:0909.3098
- Marten, A., Matthews, H. E., Owen, T., Moreno, R., Hidayat, T., & Biraud, Y. 2005, *A&A*, 429, 1097
- Mason, B. S., Weintraub, L., Sievers, J., Bond, J. R., Myers, S. T., Pearson, T. J., Readhead, A. C. S., & Shepherd, M. C. 2009, *ApJ*, 704, 1433
- Mauch, T., Murphy, T., Buttery, H. J., Curran, J., Hunstead, R. W., Piestrzynski, B., Robertson, J. G., & Sadler, E. M. 2003, *MNRAS*, 342, 1117
- Murphy, T., et al. 2009, arXiv:0911.0002
- Negrello, M., Perrotta, F., González-Nuevo, J., Silva, L., De Zotti, G., Granato, G. L., Baccigalupi, C., & Danese, L. 2007, *MNRAS*, 377, 1557
- Niemack, M. D. 2008, Ph.D. thesis, Princeton University
- Niemack, M. D., et al. 2008, *J. Low Temp. Phys.*, 151, 690
- Nolta, M. R., et al. 2009, *ApJS*, 180, 296
- Peebles, P. J. E. 1980, *The large-scale structure of the universe* (Princeton University Press)
- Press, W. H., Teukolsky, S. A., Vetterling, W. T., & Flannery, B. P. 2007, *Numerical Recipes: The Art of Scientific Computing*, 3rd edn. (Cambridge University Press)
- Reichardt, C. L., et al. 2009a, *ApJ*, 701, 1958
- , 2009b, *ApJ*, 694, 1200
- Righi, M., Hernández-Monteagudo, C., & Sunyaev, R. A. 2008, *A&A*, 478, 685
- Sayers, J., et al. 2009, *ApJ*, 690, 1597
- Scott, D. & White, M. 1999, *A&A*, 346, 1
- Sehgal, N., et al. 2010, *ApJ*, 709, 920
- Seljak, U., Burwell, J., & Pen, U. 2001, *Phys. Rev. D*, 63, 063001
- Sharp, M. K., et al. 2009, arXiv:0901.4342
- Sievers, J. L., et al. 2009, arXiv:0901.4540
- Sunyaev, R. A. & Zel'dovich, Y. B. 1970, *Comments on Astrophysics and Space Physics*, 2, 66
- Swetz, D. S., et al. 2008, in *Proc. SPIE*, ed. W. D. Duncan, W. S. Holland, S. Withington, & J. Zmuidzinas, Vol. 7020 (SPIE), 702008
- Switzer, E. R. 2008, Ph.D. thesis, Princeton University
- Switzer, E. R., et al. 2008, in *Proc. SPIE*, ed. A. Bridger & N. M. Radziwill, Vol. 7019 (SPIE), 70192L
- Tegmark, M. 1997, *ApJ*, 480, L87
- Tegmark, M. & de Oliveira-Costa, A. 1998, *ApJ*, 500, L83
- Thornton, R. J., et al. 2008, in *Proc. SPIE*, ed. W. D. Duncan, W. S. Holland, S. Withington, & J. Zmuidzinas, Vol. 7020 (SPIE), 70201R
- Toffolatti, L., Argüeso Gomez, F., De Zotti, G., Mazzei, P., Franceschini, A., Danese, L., & Burigana, C. 1998, *MNRAS*, 297, 117
- Veneziani, M., et al. 2009, *ApJ*, 702, L61
- Viero, M. P., et al. 2009, arXiv:0904.1200
- Vikhlinin, A., et al. 2009, *ApJ*, 692, 1060
- Weiland, J. L., et al. 2010, arXiv:1001.4731
- White, M. J. & Majumdar, S. 2004, *ApJ*, 602, 565
- Wright, A. E., Griffith, M. R., Burke, B. F., & Ekers, R. D. 1994, *ApJS*, 91, 111
- Wright, E. L., et al. 2009, *ApJS*, 180, 283
- Zhao, Y., et al. 2008, in *Proc. SPIE*, ed. W. D. Duncan, W. S. Holland, S. Withington, & J. Zmuidzinas, Vol. 7020 (SPIE), 70200O